

Structural Characterization of Single-Stranded DNA Monolayers Using Two-Dimensional Sum Frequency Generation – Supplemental Information

Jia-Jung Ho, David R. Skoff, Ayanjeet Ghosh, Martin T. Zanni

Table of Contents

Methods	2
1.1 - 1D Spectroscopy Setups	2
1.1.1 Transmission FTIR Spectroscopy (FTIR).....	2
1.1.2 Infrared Reflection Absorption Spectroscopy (IRRAS).....	2
1.1.3 Raman Spectroscopy	2
1.2 - 2D Spectroscopy Setups	3
1.3 - 2D SFG Simulation Models	4
Result	6
2.1 - Monolayer Characterization with X-Ray Photoelectron Spectroscopy (XPS)	6
2.1.1 XPS Spectra for 2D SFG Samples	7
2.1.2 XPS Spectra for 1D SFG Samples	8
2.2 - Spectral Features in 2D Spectra	9
2.3 - Visible Line Widths Convolute into 2D SFG	11
2.4 - Waiting Time Dynamics	11
Discussion	15
3.1 - DFT Calculation and Vibration Mode Decomposition Analysis	15
3.2 - Two Cases That Could Generate Matched IRRAS and FTIR Spectra	16
3.3 - Determination of Absolute Orientation	17
3.4 - 2D SFG Absolute Signal Size	20
3.5 - 1D SFG Absolute Signal Size	21
3.6 - Simulated 2D SFG Absolute Signal Size as Function of ψ	23
3.7 - Peak Sign and Intensity Analysis of HD 2D SFG	23
3.8 - Footprint Estimation of Monolayer Film	25
Supplemental Information References	28

Methods

1.1 - 1D Spectroscopy Setups

1.1.1 Transmission FTIR Spectroscopy (FTIR)

Transmission FTIR spectra were collected using a Thermo Scientific Nicolet iS10 spectrometer. Spectra were collected at 2 cm^{-1} resolution and 50 scans were averaged. The spectrometer was purged with dry air to eliminate water vapor lines. D_2O CaCl_2 -TE buffer solution was used as a background for the $(\text{dT})_{25}$ -SH in D_2O buffer sample. An air background was used for the dehydrated $(\text{dT})_{25}$ -SH sample.

1.1.2 Infrared Reflection Absorption Spectroscopy (IRRAS)

IRRAS spectra were collected using a Bruker Vertex 70 FTIR spectrometer with a Pike Technologies VeeMax II variable-angle single-bounce reflection attachment. The spectra were detected with a liquid nitrogen cooled HgCdTe detector. IR light was *p*-polarized and the angle of incidence was 50° from surface normal. The spectra were collected with 2 cm^{-1} resolution and 1000 scans were averaged. A bare gold sample was used as a background for the $(\text{dT})_{25}$ -SH monolayer on gold sample.

1.1.3 Raman Spectroscopy

Raman spectra were collected with a Thermo Scientific DXR Raman Microscope. The 633 nm laser line was used as the excitation wavelength. A high-resolution grating was used to give 2 cm^{-1} resolution. The laser power was 8 mW. Ten scans were averaged with each scan being collected for 10 seconds.

Because our 2D SFG experiments depend not only on the transition dipole moments of each mode, but also on the Raman polarizability, we have collected the Raman spectrum of the dehydrated $(\text{dT})_{25}$ -SH film (Fig. 3, blue). The signal was too small to easily measure the monolayer directly, but we believe the result will be similar since we have already seen that the IR spectrum of the dehydrated film closely matches the monolayer sample.

The Raman spectrum exhibits the most intense feature at 1667 cm^{-1} with a shoulder at about 1690 cm^{-1} . We assign these two modes to T2 and T1, respectively since they are similar to those in the IR spectra and because of the relative intensities, since Raman and IR intensities are often anti-correlated. DFT calculations also predict anti-correlation of the IR and Raman intensities for the T1 and T2 modes. We do not see a strong feature for T3 and so we conclude that T3 has a small polarizability.

1.2 - 2D Spectroscopy Setups

The 2D SFG and 2D IR spectrometers are similar to those that have been previously described.¹ Briefly, a regeneratively-amplified Ti:Sapphire laser (Coherent Libra) output femtosecond pulses (800 nm, ~50 fs FWHM, ~4 mJ/pulse) at a 1 kHz repetition rate. Three quarters of the 800 nm output (3 mJ/pulse) pumped an optical parametric amplifier (TOPAS) followed by a home-built AgGaS₂ difference frequency generation setup to produce about 30 μ J/pulse of mid-IR light centered at ~5.8 μ m. A CaF₂ window was used to split the mid-IR pulse into a pump and probe beam path. About 95% of the light was sent through a Ge acousto-optic pulse shaper to create the E₁ and E₂ pump mid-IR pulses for both the 2D SFG and 2D IR experiments. The remaining 5% was used as the E₃ probe mid-IR pulse.

For the 2D SFG experiments, the 800 nm light that was not used for mid-IR generation (1 mJ/pulse) was frequency-narrowed using a 1 nm FWHM interference filter centered at 805 nm. After filtering, the visible pulse power was 15 μ J/pulse. The visible pulse and mid-IR pulses were focused using 30 cm and 20 cm lenses respectively, and overlapped at the sample as shown in Fig. 1. The angle of incidence for the visible pulse was $\theta_{vis} = 65^\circ$, and for the mid-IR pulses $\theta_{IR} = 75^\circ$ from normal. The visible pulse and all mid-IR pulses were *p*-polarized to collect a ppppp 2D SFG signal. To prevent potential sample degradation during the experiment, the sample was scanned in the *xy*-plane such that a spot on the sample was only probed for 5 minutes before changing to a new spot. The fourth-order resonant signal from DNA and the second-order non-resonant signal emitted from gold both travel in the $k_{res} = k_{non-res} = k_{vis} + k_{probe}$ direction. The second order non-resonant signal were used as local oscillator for heterodyne detection². The signal beam was re-collimated and the spatially nearby 805 nm beam was removed with a 735 nm short pass filter. This signal was sent into a Horbia Triax 320 monochromator and frequency dispersed onto a Princeton Instruments PIXIS 400 CCD detector. The t_1 coherence period was scanned using the mid-IR pulse shaper from 0 fs to 1500 fs in 50 fs steps. Each t_1 time point was averaged on the CCD detector for 5 seconds (or 5000 laser shots). Collecting all t_1 time points to give one 2D SFG scan took about 5 minutes, and many scans were averaged to give the final 2D SFG spectra. A two-frame phase cycling scheme and rotating frame frequency of 1550 cm⁻¹ was used so that the 50 fs steps still sample the free-induction decay at more than the Nyquist frequency. The time delay between the visible and mid-IR probe pulse, t_{vis} , was 0 fs.

For the solution 2D IR experiments, the pump and probe pulses were all parallel polarized to collect a ZZZZ signal. All pulses were focused onto the sample using a 2 inches parabolic mirror in a pump-probe beam geometry. The t_1 coherence period was scanned using the mid-IR pulse shaper to create a pump pulse pair,

E_1 and E_2 , with time separations from 0 fs to 1500 fs in 50 fs steps. The same laser source, pulse shaper and delays were used for both the 2D SFG and solution 2D IR measurements so that they could be directly compared. In this geometry the 2D IR signal is generated in the direction of the E_3 probe pulse, which acts to heterodyne the signal. The ω_3 frequency axis was resolved by sending the signal into a monochromator (150 mm focal length) and frequency dispersing the signal with a 75 grooves/mm grating blazed for 8 μm light onto a 32-pixel HgCdTe (MCT) array detector. Because a 32-pixel MCT array was used the range of the ω_3 frequency axis was from 1586-1713 cm^{-1} , the edge of which is represented by dashed lines in Fig. 4c.

The 2D IR experiments on dehydrated (dT)₂₅-SH were collected with perpendicularly polarized pump and probe pulses (ZZYY) in order to minimize interference between the signal and pump light scattered in the signal direction. The t_1 coherence period was scanned to 2520 fs because the sample had a longer free-induction decay, which gives a slightly higher frequency resolution along the pump axis. The ω_3 frequency axis was resolved by sending the signal into a monochromator (150 mm focal length) and frequency dispersing the signal with a 75 grooves/mm grating blazed for 8 μm light onto a 64-pixel MCT array. A 64-pixel MCT array allowed the collection of a larger range on the ω_3 frequency axis, and the entire range in Fig. 4b (1575-1800 cm^{-1}) was collected.

1.3 - 2D SFG Simulation Models

We simulate the 2D SFG spectra of ssDNA monolayers in two ways. The first model we present is an uncoupled base model. In this model, we assume no coupling between thymine bases so that a single thymine base is all that is necessary to obtain relative intensity between peaks, the peak signs, and the peak patterns. The purpose of this model is to approximate the single base orientation relative to the surface by matching simulations to experimental spectra. As justified below, all 2D SFG simulations use the DFT calculation results for dehydrated deoxythymidine because the oligo(dT) monolayers are found to have vibrational characteristics of dehydrated oligo(dT) films.

In the uncoupled base model, the 2D SFG spectrum is simulated in the following way. A diagonalized two-exciton Hamiltonian for a single thymine base is constructed from the one-exciton, two-exciton, and combination band frequencies. In the 1600-1750 cm^{-1} range, there are three normal modes that we refer to as T1, T2, and T3. The anharmonicity of the two-exciton and combination bands were calculated with anharmonic frequency calculations.^{3,4} However, because DFT calculations result in well-known frequency discrepancies between calculated and experimental values, we use the experimental values for the one-exciton vibrational frequencies in our simulations. The transition dipole moment vectors between the vibrational ground state and first-excited state for each of the three normal modes are taken from the DFT calculation. We employ the

harmonic approximation to get the transition dipole moment vectors between the one and two-exciton states by multiplying the corresponding ground to one-exciton state transition dipole moment vector by $\sqrt{2}$. The Raman polarizability tensors for each normal mode from the DFT calculation are also used. All five incident beams are set to be p -polarized and all beam incident angles are set to 90° in the simulation because electric field components that project parallel to the surface effectively cancel in the experiment, which is the basis for the metal-surface selection rule.^{5,6}

The second model we construct to simulate the 2D SFG spectra includes coupling between multiple thymine bases. In this simulation, we are still only concerned with the T1, T2, and T3 modes of each thymine base. We model the coupling between four bases, because we find this model adequately reproduces the major features of the experimental spectra. Coupling terms are included between every pair of bases with the coupling constants between any two bases calculated using transition dipole coupling. With four bases (base A, B, C and D) and three local modes per base (T1, T2, and T3) there are twelve local modes of interest that are transformed into twelve exciton modes in our model (i.e. the one-exciton block of the Hamiltonian is of size 12-by-12). Before diagonalization, the local mode frequencies are along the diagonal and coupling terms, β , are off-diagonal elements. The local mode anharmonicity of the two-exciton and combination bands are taken from the DFT calculations. Coupling between degenerate local modes will cause much larger shifts than coupling between local modes separated by $\sim 40 \text{ cm}^{-1}$, and so we neglect coupling constants between different types of local modes (e.g. between T1 and T2).

For all the simulated spectra, we apply diagonal disorder that shifts the one-exciton, two-exciton, and combination band frequencies to simulate inhomogeneous lineshapes. We applied frequency shifts to all local modes randomly from a Gaussian distribution of 13 cm^{-1} FWHM. 10^4 runs of the simulation were combined to smoothly sample the Gaussian distribution. On 20% of the 10^4 runs, the frequency shifts were correlated between the T1, T2, and T3 modes to match the experimental cross peak lineshape.^{7,8} The resulting compilation of stick spectra was smoothed by convolution with a Gaussian lineshape of 10 cm^{-1} FWHM. Last, the simulated spectrum was convoluted along the probe axis with a Lorentzian lineshape of 15 cm^{-1} FWHM to simulate the effects of the filter used to narrow the visible pulse bandwidth.

Result

2.1 - Monolayer Characterization with X-Ray Photoelectron Spectroscopy (XPS)

We did not collect the XPS spectra for samples before 2D SFG experiments to avoid potential sample degrading. After the exposure to air during the 2D SFG experiments, the XPS data of 2D samples may have some contamination. However, we took the XPS spectra for a set of freshly prepared samples. We also took 1D SFG of these samples to make sure they are comparable to previous 2D samples.

XPS spectra were collected using a Thermo Scientific K-Alpha XPS instrument. Data was collected with a 400 μm spot size and 50 eV pass energy resulting in a 0.82 eV resolution. For quantitative surface coverage analysis, we followed a previously described method for thiolated poly(thymine) ssDNA monolayers on gold⁹. In accordance with this previous method, the atomic density of nitrogen was used to determine the surface coverage of the ssDNA because surface contamination typically will not affect the N 1s XPS peak. The atomic density of nitrogen relative to the atomic density of gold was determined using the N 1s and Au 4f_{7/2} peaks. This was converted to surface coverage of DNA by accounting for film thickness, atomic density of gold, and number of N atoms per DNA molecule as previously described⁹.

Briefly, to determine the film thickness we use the following equation:

$$I_{Au} = I_{Au}^0 \exp \left[-\frac{t}{L_{Au}} \right] \quad \text{Eq. S1}$$

I_{Au} : Observed intensity of gold substrate

I_{Au}^0 : Intensity from bare gold substrate

t : Film thickness

L_{Au} : average practical Effective Attenuation Length (EAL)

And the relative atomic density can be calculated by:

$$\frac{N_x}{N_{Au}} = \frac{I_x T_{Au} \sigma_{Au} L_{Au}^Q \exp[-t/L_{Au}]}{I_{Au} T_x \sigma_x L_x^Q (1 - \exp[-t/L_x])} \quad \text{Eq. S2}$$

I_x : Intensity of element X

T_x : Transmission function of element X

σ_x : Photoelectric cross section of element X

L_{Au} : EAL for quantitative analysis

These parameters were taken from previous publication⁹, except T_X , which is pre-normalized by the manufacture. As a result, we can neglect transmission function part in Eq. S2.

To calculate the element and DNA coverage, we assume the density (ρ_{Au}) of gold is $19.28g/cm^3$. Thus we can calculate the absolute atomic density of nitrogen atom:

$$N_N \left[\frac{atoms}{cm^2} \right] = \left(\frac{N_N}{N_{Au}} \right) * \rho_{Au} \left[\frac{atoms}{cm^3} \right] * t [cm] \quad \text{Eq S3}$$

2.1.1 XPS Spectra for 2D SFG Samples

In figure S1, we show the XPS spectra of oligo(dT) monolayer samples and summarize their properties in table S1.

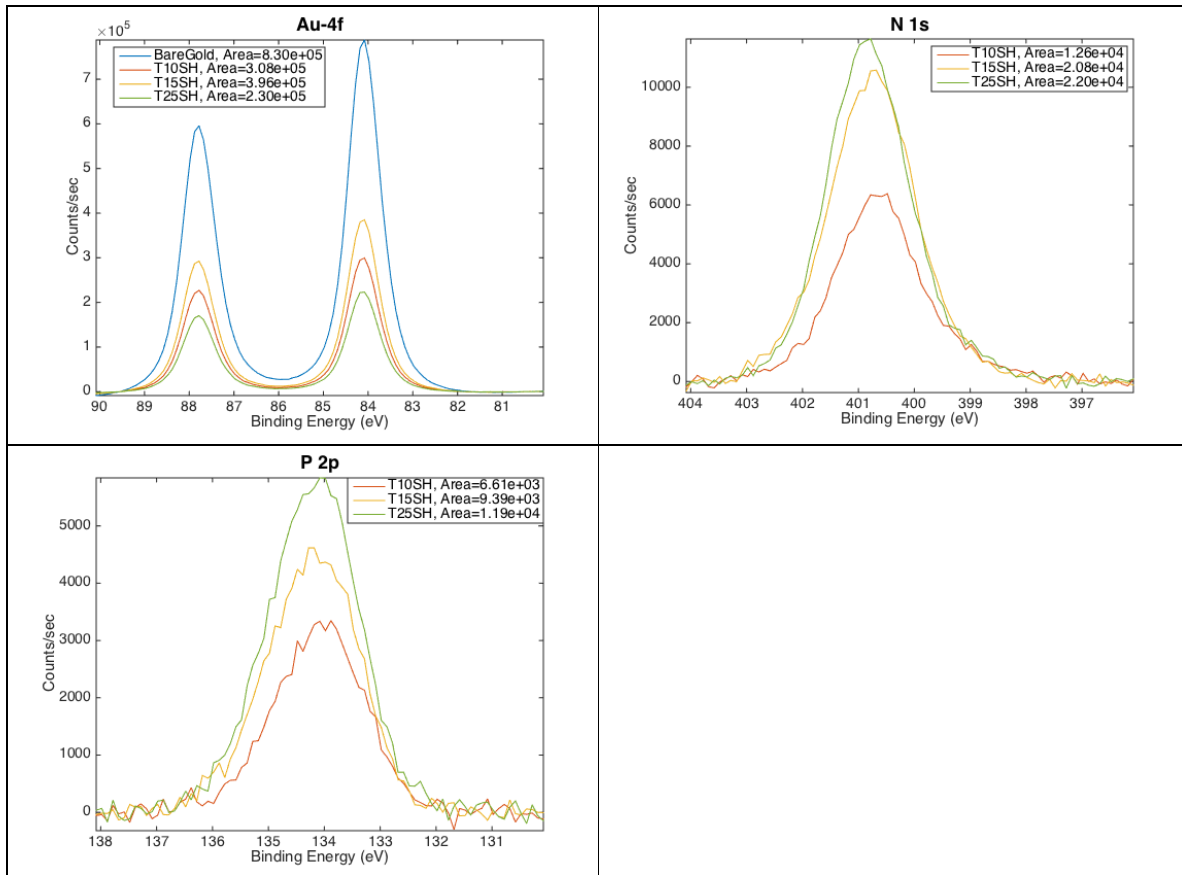


Figure S1 XPS spectra of the Au 4f, N 1s, and P 2p regions of oligo(dT) monolayers on gold, which was used for 2D SFG experiments. The peak areas are noted in figure legends.

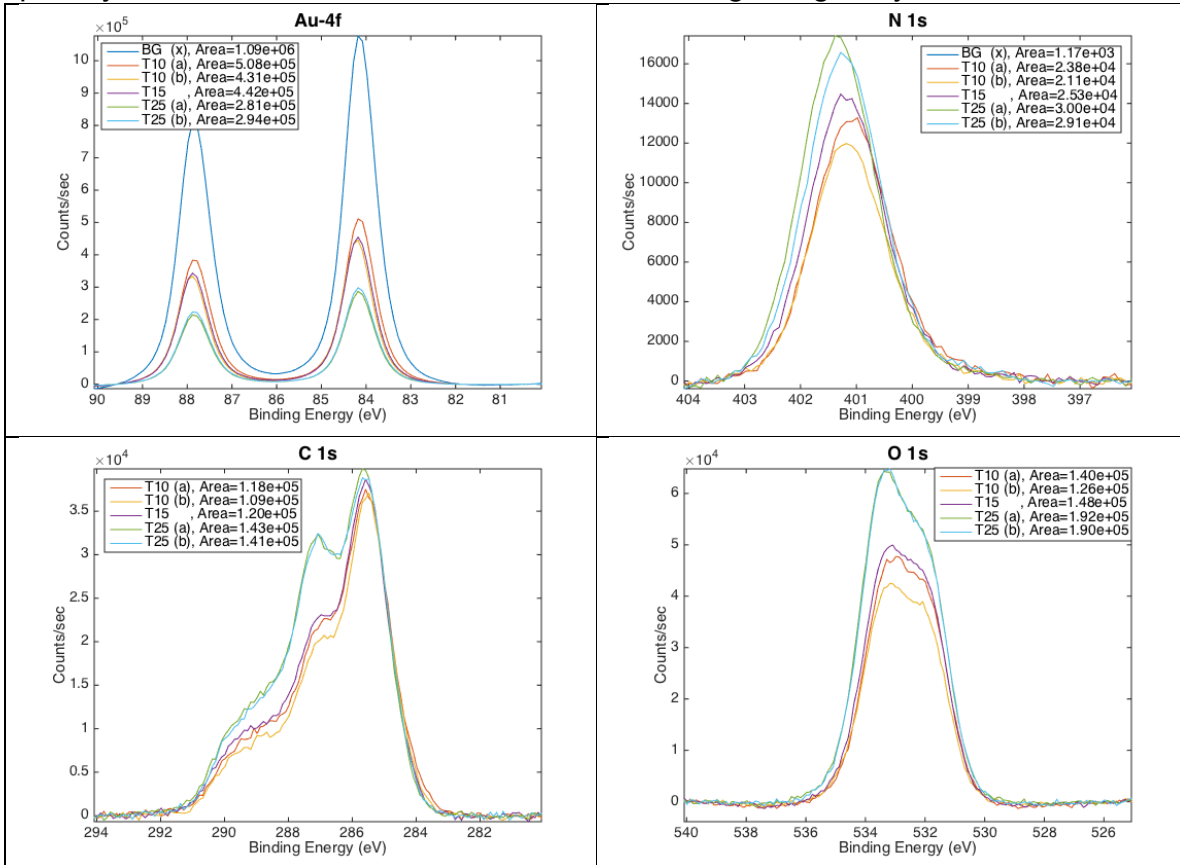
2D	Thickness (nm)	$\frac{N_N}{N_{Au}}$	$N_N \left(\frac{atoms}{cm^2} \right)$	$N_{DNA} \left(\frac{Molecule}{cm^2} \right)$
T10	3.825	0.061	$1.381 * 10^{15}$	$6.90 * 10^{13}$
T15	2.855	0.119	$2.005 * 10^{15}$	$6.68 * 10^{13}$
T25	4.951	0.095	$2.772 * 10^{15}$	$5.54 * 10^{13}$

Table S1: Surface coverage of DNA monolayers for 2D SFG experiments

One interesting fact is that the thickness of (dT)₁₅-SH is thinner than (dT)₁₀-SH. This could be caused by two possible reasons. On one hand, the sample was exposed in air during 2D SFG data acquisition so it may be contaminated. On the other hand, the monolayer packing may be different for (dT)₁₅-SH sample. We did observe that the intensity ratio between T1 and T2 is slightly different from (dT)₁₅-SH and (dT)₂₅-SH. This suggests slightly different bases orientation. The orientation difference of DNA bases could induce different monolayer packing.

2.1.2 XPS Spectra for 1D SFG Samples

In this set of data, we provide the XPS of freshly made samples. The result is consistent with the 2D SFG samples. We also calculate the O/N atomic ratio. The ratio is very close to theoretical ratio, which suggests less than single water, if any, per thymine base. This result bolsters our modeling using dehydrated molecule.



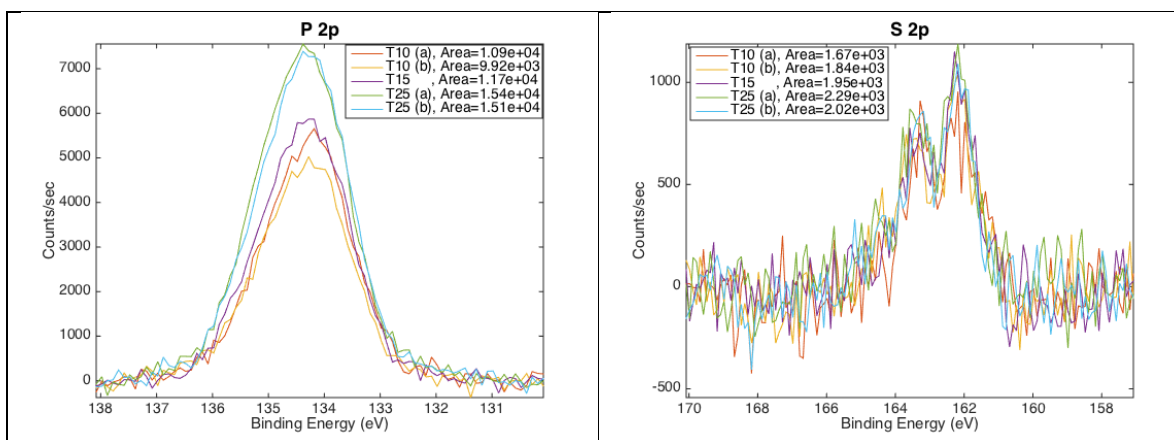


Figure S2: XPS spectra of the freshly made oligo(dT) monolayers on gold. . The peak areas are noted in figure legends.

1D	Thickness (nm)	$\frac{N_N}{N_{Au}}$	$N_N \left(\frac{atoms}{cm^2} \right)$	$N_{DNA} \left(\frac{Molecule}{cm^2} \right)$	O/N (3.5)
T10 (a)	2.945	0.102	$1.769 * 10^{15}$	$8.84 * 10^{13}$	3.76
T10 (b)	3.580	0.081	$1.706 * 10^{15}$	$8.53 * 10^{13}$	3.85
T15	3.483	0.098	$2.020 * 10^{15}$	$6.73 * 10^{13}$	3.76
T25 (a)	5.230	0.097	$2.976 * 10^{15}$	$5.95 * 10^{13}$	4.19
T25 (b)	5.055	0.095	$2.827 * 10^{15}$	$5.65 * 10^{13}$	4.27

Table S2: Thickness, surface coverage, and relative atomic ratio of freshly made DNA monolayers for 1D SFG experiments.

2.2 - Spectral Features in 2D Spectra

We interpret the spectrum shown in Fig. 4b, for which we have labeled each peak, as follows. The negative peak that appears at the same pump frequency (1715 cm^{-1}), but lower probe frequency (1687 cm^{-1}) is assigned as the overtone peak of the T1 mode (O_1). The T2 mode gives a negative fundamental peak along the diagonal of the plot at ($\omega_{\text{pump}} = 1672 \text{ cm}^{-1}$, $\omega_{\text{probe}} = 1687 \text{ cm}^{-1}$). The overtone peak of the T2 mode (O_2) is shifted to lower frequency along the probe axis (1656 cm^{-1}). Thus, in the spectrum the T1 and T2 modes give fundamental peaks with opposite signs along the diagonal of the plot. We see no clear evidence of a third peak pair along the diagonal of the 2D SFG plot that can be decisively assigned to the T3 mode. We would expect these peaks to be near the position of the T₃ and O₃ labels. This is consistent with the fact that the T3 mode appears to be weak, both in IR and Raman intensity, when dehydrated (Fig. 4a).

There are three remaining peaks in this spectrum, C_{11} , C_{21} , and C_{23} , which are cross-peaks that appear due to coupling between the T1, T2, and T3 vibrational modes. First, the positively signed peak C_{21} that appears off the diagonal between the T1 and T2 fundamental peaks at ($\omega_{\text{pump}} = 1672 \text{ cm}^{-1}$, $\omega_{\text{probe}} = 1723 \text{ cm}^{-1}$), is assigned as a cross-peak between the T1 and T2 modes. Second, the

negatively signed peak C_{23} that appears at the pump frequency of the T2 mode and probe frequency of about 1630 cm^{-1} is assigned as a cross-peak between the T2 mode and the T3 mode. The T2-T3 cross-peak is stronger than the fundamental and overtone peaks of the T3 mode (T_3 & O_3) because the cross-peak intensity depends on mode strengths of both T2 and T3. If T2 has stronger IR and Raman transitions, then the T2 mode effectively amplifies the cross-peak intensity. Last, there is a negative cross-peak (C_{11}) that appears at the pump frequency of the T1 mode and probe frequency of $\sim 1755\text{ cm}^{-1}$. This peak cannot be explained as a cross-peak for any of the T1, T2, and T3 modes discussed above. We propose that this cross-peak is due to vibrational coupling that occurs between T1 vibrational modes on neighboring thymine bases, creating T1 bright and dark states. Peak C_{11} is a cross-peak between the brightest T1 excitonic mode and dark excitonic modes. Like in the case of the T3 mode, the dark excitonic states do not show appreciable intensity along the diagonal, but the cross-peak gains strength from the T1 bright excitonic mode and can therefore appear more intensely. We explore this assignment further with simulations of coupled thymine bases shown in the Discussion section

In the case of the dehydrated film (Fig. 4c), we can clearly identify two peak pairs along the diagonal of the plot (T_1, O_1 & T_2, O_2). The higher frequency peak pair is assigned to the T1 mode. The fundamental peak from the T1 mode shows up at ($\omega_{\text{pump}} = 1713\text{ cm}^{-1}$, $\omega_{\text{probe}} = 1719\text{ cm}^{-1}$). The overtone peak (O_1) is shifted by $\sim 18\text{ cm}^{-1}$ to lower frequency along the probe axis. The second fundamental peak at ($\omega_{\text{pump}} = 1667\text{ cm}^{-1}$, $\omega_{\text{probe}} = 1677\text{ cm}^{-1}$) is assigned to the T2 mode. The overtone for the T2 mode (O_2) actually appears to be stronger in the spectrum than the fundamental peak. This is due to interference between the T2 fundamental peak and a cross-peak occurring between the T1 and T2 mode (C_{21}). The cross-peak C_{21} is at the pump frequency of T2 and probe frequency of T1, and appears as essentially a negative strip in the spectrum that extends from the T1 mode diagonal peak. The strip extends from $\omega_{\text{pump}} = 1675\text{ cm}^{-1}$ to about 1615 cm^{-1} . We suspect that the strip extends down to about 1615 cm^{-1} because the T3 mode is in this frequency region and thus we are detecting a cross-peak (C_{31}) between T1 and T3 at the lowest frequency end of the cross-peak strip. The T3 mode fundamental is likely subject to interferences, which make it appear even weaker and less intense than the overtone (O_3). Overall, the dehydrated film and monolayer are similar since they show strong peaks from T1 and T2 that are elongated along the diagonal due to inhomogeneity.

The 2D IR spectrum of $(\text{dT})_{25}\text{-SH}$ in D_2O $\text{CaCl}_2\text{-TE}$ buffer (Fig. 4d) is less comparable to the monolayer spectrum because it shows three prominent and sharper peak pairs along the diagonal (T_1, O_1 & T_2, O_2 & T_3, O_3). We assign the highest frequency peak pair (T_1, O_1), at $\omega_{\text{pump}} = 1691\text{ cm}^{-1}$, to the T1 mode fundamental and overtone. The peak pair at $\omega_{\text{pump}} = 1663\text{ cm}^{-1}$ is assigned to the T2 mode (T_2, O_2). The T3 mode is strong in this spectrum with its fundamental and overtone peaks at $\omega_{\text{pump}} = 1625\text{ cm}^{-1}$ (T_3, O_3). Cross-peaks are present between all three vibrational modes. There is a weak cross-peak (C_{21}) between

the T1 and T2 modes as observed in the monolayer and dehydrated films. Another strong cross-peak (C_{23}) appears on the other side of the diagonal between both T1-T3 and T2-T3. The strongest cross-peak (C_{32}) appears below the diagonal between the T2 and T3 modes at ($\omega_{\text{pump}} = 1629 \text{ cm}^{-1}$, $\omega_{\text{probe}} = 1666 \text{ cm}^{-1}$). This cross-peak is not apparent in the monolayer and dehydrated film spectra, but is strong here because both the T2 and T3 transition dipoles are large when hydrated. The 2D IR spectrum of hydrated (dT)₂₅-SH does closely resemble the spectrum of thymidine 5'-monophosphate in D₂O buffer that has previously been reported.¹⁰ This suggests that intramolecular base-to-base coupling effects do not have a large influence on the 2D IR spectrum in the hydrated case.

In summary, we have shown that there are large differences between 2D SFG spectra of (dT)₂₅-SH monolayers and 2D IR spectra of hydrated and dehydrated (dT)₂₅-SH (waiting time experiments also show differences, see Fig. S3). The 2D SFG spectra have the added complexity that fundamental peaks may appear as either positive or negative along the diagonal of the plot, which is not possible in 2D IR measurements. Qualitatively, the 2D SFG signal shows that the thymine bases are ordered such that the T1 and T2 mode have fourth-order susceptibilities of opposite sign. This requires the T1 and T2 transition dipole moment vectors to project onto the surface normal in opposite directions.

2.3 - Visible Line Widths Convolute into 2D SFG

Another difference between 2D SFG and 2D IR spectroscopy is in the way that the signals are detected. Both are heterodyne detected, but the 2D SFG experiment also contains a visible laser pulse. We are detecting the 2D SFG signal in the frequency domain, meaning that we use a narrow band visible pulse and a monochromator to Fourier transform the emitted free-induction decay into a spectrum. As a result, the signal along the probe axis of the 2D SFG spectrum is convoluted with the bandwidth of the visible pulse. We measured the probe spectrum and got a 15 cm⁻¹ Lorentzian, resulting in a broadening along this axis. Only femtosecond pulses are used in the 2D IR pulse sequence and so there is very little broadening in the 2D IR spectra. The separation between the fundamental and overtone peaks along the probe axis is due to the anharmonicity of the vibrational mode, but because of the broadening along the probe axis, the separation between the two peak is exaggerated. Thus, the actual anharmonic shift is much closer to the apparent peak separation in the 2D IR spectra, which is ~20 cm⁻¹. For this reason, it is better to use the pump frequency axis to judge the mode frequencies in the 2D SFG experiment. This effect was also discussed in our previous paper on the 2D SFG spectra of a peptide monolayer.¹

2.4 - Waiting Time Dynamics

Sub-picosecond timescale dynamics are probed in 2D SFG and 2D IR experiments using the waiting time, t_2 . The intensities and 2D lineshapes of the peaks in the 2D SFG spectra change with waiting time, indicating both lifetime effects and structural dynamics (Fig. S3a-b). We observe that the fundamental and overtone of the T1 mode (T_1, O_1) decay faster than the T2 mode (T_2, O_2). Also, the cross-peak between the T1 and T2 mode (C_{21}) shows a slight increase in intensity, while cross-peaks C_{23} and C_{11} decrease. In 2D IR experiments, we typically account for lineshape and intensity changes as a function of t_2 , with structural fluctuations, energy transfer, and chemical exchange.^{11,12} All of these phenomena can be measured with 2D SFG experiments as well, although some interesting differences exist between the two experiments. For instance, in a 2D SFG experiment, energy may be transferred from an SFG-active mode to an SFG-inactive mode, and vice versa. This could cause peaks to broaden or narrow with waiting time. Structural fluctuations can change the direction of transition dipole moment vectors or Raman tensors relative to the surface, which in turn could make the mode more or less intense even without a change in population. In sum, these effects can result in complex frequency dependence across a peak in 2D SFG spectra.

One example from our data is the T2 mode fundamental peak that becomes narrower at the center of the peak ($\omega_{\text{pump}} = 1672 \text{ cm}^{-1}$) while broadening out at the higher frequency end ($\omega_{\text{pump}} \sim 1700 \text{ cm}^{-1}$) as t_2 increases. This helps reveal an even more inhomogeneous lineshape for peak T_2 that clearly interferes with peak T_1 at early waiting times. Another example is cross-peak C_{21} which becomes narrower along the probe axis going from $t_2 = 0 \text{ fs}$ to 500 fs . In 2D IR, spectral diffusion causes narrow inhomogeneous lineshapes to broaden along the probe axis with waiting time, not the reverse. In 2D SFG, narrowing along the probe axis is possible. Accurately modeling the waiting time dynamics in 2D SFG and 2D IR experiments to determine the cause of spectral changes is difficult and is not our goal here. We show the waiting time experiments to compare and contrast dynamic observables in 2D SFG with the 2D IR measurements discussed below.

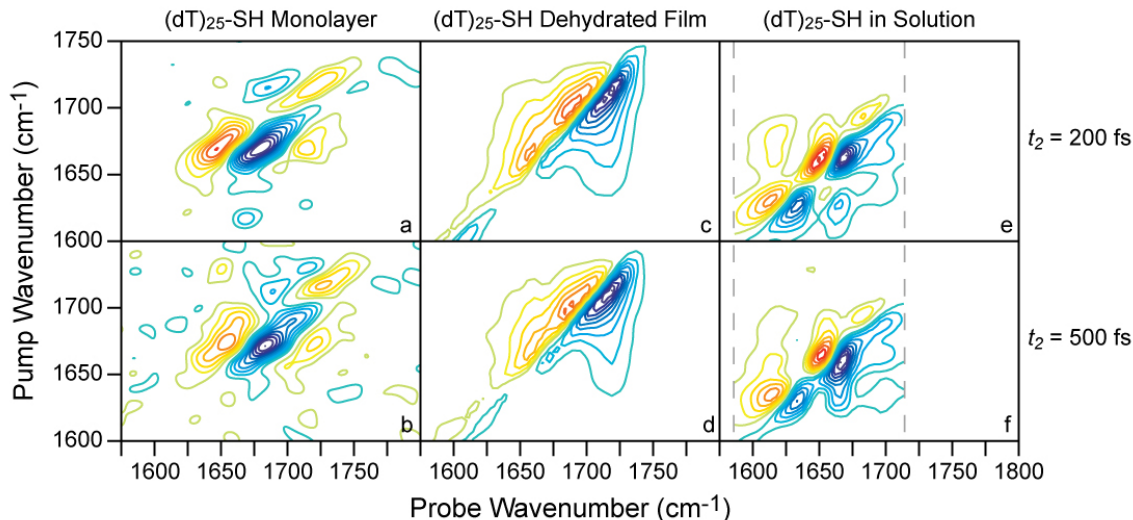


Figure S3: 2D SFG and 2D IR spectra of (dT)₂₅-SH at $t_2 = 200$ & 500 fs. (a) 2D SFG spectrum of a (dT)₂₅-SH monolayer on gold. (b) 2D IR spectrum of a dehydrated (dT)₂₅-SH film. (c) 2D IR spectrum of (dT)₂₅-SH in D₂O CaCl₂-TE buffer.

In contrast to the (dT)₂₅-SH monolayer, we observe that in the t_2 series of the dehydrated (dT)₂₅-SH film, the T₁ and T₂ fundamental peaks along the diagonal remain relatively unchanged in terms of relative intensity and linewidth (Fig. S3c-d). The persistent narrow, inhomogeneous lineshapes for peaks T₁ and T₂ shows that frequency correlation relaxations on the 500 fs time scale are not significantly large in this sample. This is consistent with the fact that the sample is dehydrated, because spectral diffusion is often associated with dynamics of the solvent interacting with the chromophore in 2D IR experiments.¹³ Lack of solvent therefore minimizes this effect. We do observe that the cross peak between the T₁ and T₂ modes (peak C₂₁) remains strong for all t_2 times, as it does in the 2D SFG spectra. However, peak C₂₁ does not narrow along the probe axis in the 2D IR spectra. Peak C₂₁ changes along the pump axis as it does not extend as far in the $t_2 = 200$ and 500 fs spectra. We interpret the change as a decay of the cross-peak between the T₁ and T₃ modes that occurs at the low frequency end of the strip ($\omega_{\text{pump}} \sim 1625$ cm⁻¹). Overall, the spectral changes in the dehydrated (dT)₂₅-SH film are less dramatic, which is reasonable for a sample that lacks solvation fluctuations.

As was the case for the dehydrated film, the peak pairs along the diagonal of the 2D IR plots for (dT)₂₅-SH in buffer (T₁, O₁ & T₂, O₂ & T₃, O₃), stay relatively constant as a function of t_2 (Fig. S3e-f). There is a small relative increase in the T₁-T₂ cross-peak (C₂₁) going from $t_2 = 0$ to 500 fs as we observed for the (dT)₂₅-SH monolayer. The T₁-T₃ cross-peak below the diagonal also increases in intensity, unlike the trend in the dehydrated (dT)₂₅-SH film. The solution spectra show a more intense cross-peak (C₂₃) above the diagonal compared to the monolayer and dehydrated film, and this peak broadens as a function of waiting time. Compared to the dehydrated film, the 2D IR spectra of hydrated (dT)₂₅-SH

changes much more with waiting time, which highlights the role of solvation dynamics on the 500 fs time scale.

In summary, we see that ssDNA experiences ultrafast dynamics in monolayers, in dehydrated films, and in solution samples. Differences exist not only because of variation in hydration level, but also because of intrinsic differences between 2D SFG and 2D IR experiments.

Discussion

3.1 - DFT Calculation and Vibration Mode Decomposition Analysis

To simulate 2D SFG spectra, the vibrational transition dipole moment vectors, Raman polarizability tensors, one-exciton, two-exciton, and combination band frequencies for the vibrational modes of the molecule must be known. To determine these parameters we performed density functional theory (DFT) calculations using Gaussian '09.³ Even though we are investigating oligo(dT), our intention is to accurately simulate the vibrational modes of just the thymine base. We are concerned with simulating 2D SFG spectra in the 1600-1750 cm^{-1} region, which is dominated by the C=O & C=C stretching modes of the thymine base. Vibrational contributions from the sugar moiety and phosphate backbone do not contribute in this region and are not modeled.¹⁴ It has previously been shown that the thymine base vibrational modes in DNA can be accurately modeled using methylated DNA bases to reduce computational cost.¹⁵ Also, thymidine has been successfully used to model base vibrational modes of TMP.¹⁰ Therefore, DFT calculations were carried out on deoxythymidine using the B3LYP functional and 6-311G(d,p) basis set. Hessian calculations were performed after geometry optimizations to get the anharmonic corrected mode frequencies. To match our experiments, the H atom attached to the N3 atom in the thymine ring was replaced in the calculation with a D atom. We also performed calculations at the same level of theory, on deoxythymidine with three D_2O molecules associated with the carbonyl and N3-D groups, as has been done previously, to explore the difference between hydrated and dehydrated measurements.¹⁰

The optimized geometries and transition dipole moment vectors for both hydrated and dehydrated deoxythymidine are shown in Fig. 2. Transition dipole moment vectors are shown for the three normal modes of interest in this paper that are in the 1600-1750 cm^{-1} range. These normal modes are described below and referred to as T1, T2 and T3 in descending order of frequency.

T1	Hydrated	Dehydrated
C2=O2	60%	60%
C4=O4	16%	33%
C5=C6	9%	1%

T2	Hydrated	Dehydrated
C2=O2	4%	28%
C4=O4	40%	54%
C5=C6	33%	5%

T3	Hydrated	Dehydrated
C2=O2	12%	2%
C4=O4	10%	1%
C5=C6	63%	80%

Table S3: Percentage of vibrational mode decomposition into the three major local modes: C2=O2, C4=O4, and C5=C6.

Normal mode analysis of hydrated deoxythymidine (Fig. 2) shows that the T1 mode is 60% C2=O2 stretch in-phase with 16% C4=O4 stretch and 9% N3-D bending. The transition dipole moment vector of the T1 mode is roughly parallel to the C2=O2 bond axis, reflecting the larger contribution of the C2=O2 stretch to the T1 normal mode. The C2=O2 and C4=O4 stretches are out-of-phase in the T2 mode, with 4% C2=O2, 40% C4=O4, and 33% C5=C6 stretching and a transition dipole moment vector that is roughly parallel to C4=O4. The main contributions to the T3 mode are the C5=C6 stretching and C6-H bending motions.

Dehydrated (dT)₂₅-SH has a very different FTIR spectrum (Fig. 3, blue line). There is a major peak at 1700 cm⁻¹, a second large overlapping peak at 1667 cm⁻¹, and a third vibrational peak that is a small shoulder in this spectrum but more prevalent in hydrated FTIR. DFT calculations show that when deoxythymidine is dehydrated, the normal modes and transition dipole moment vectors are different than in the hydrated case (Fig. 2). When dehydrated, the T1 mode is still composed of in-phase C=O stretching, but the contribution of each C=O is more equal, as evidenced by the direction of the transition dipole moment vector that is almost along the direction of the vector sum of the C2=O2 and C4=O4 axes. The T2 mode is not altered as much by dehydration. Its transition dipole moment vector is rotated 15° from the hydrated case, because the T2 normal mode now consists of 28% C2=O2 and 54% C4=O4 out-of-phase stretches. The T3 mode still mainly has contributions from C5=C6 stretch and C6-H bend, but less C=O stretching that results in a large change in dipole direction

3.2 - Two Cases That Could Generate Matched IRRAS and FTIR Spectra

In the figure 3, we see that the FTIR of dehydrated (dT)₂₅-SH matches its IRRAS spectrum. We know IRRAS has a well-known surface selection rule that the signal only reports the transition dipole projection onto surface normal while the intensity of FTIR proportional to the vector length of transition dipoles. As a result the spectrum similarity implies the following result:

$$|\vec{V}_2|^2 : |\vec{V}_1|^2 = \left\langle (\vec{V}_{2,z})^2 \right\rangle_{Avg} : \left\langle (\vec{V}_{1,z})^2 \right\rangle_{Avg} \quad \text{Eq. S4}$$

In equation S4, \vec{V}_i refers to the i-th transition dipole vector while $\vec{V}_{i,z}$ is its projection onto surface normal. On the right hand side of equation S4, the ensemble average refers to the molecular orientation distribution on the surface.

Given two modes (e.g. T1 and T2 modes of sample), the relative orientation can be shown as the following figure:

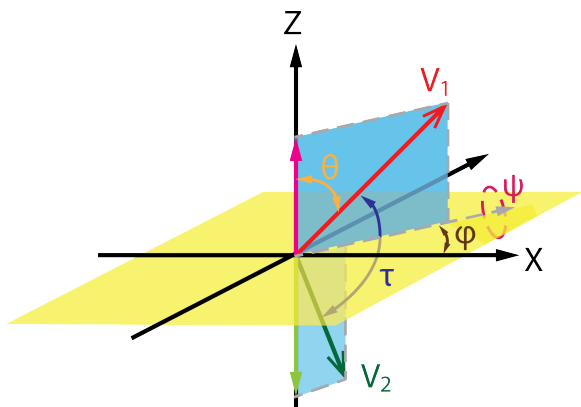


Figure S4 coordinate system for a two modes system.

If the molecule is isotropically distributed, the peak ratio of IRRAS spectrum can be calculated by taking the ensemble average of the right hand side of equation 1:

$$\begin{aligned}
 & \int (\vec{V}_{2,z})^2 \sin \theta \, d\theta \, d\varphi \, d\psi : \int (\vec{V}_{1,z})^2 \sin \theta \, d\theta \, d\varphi \, d\psi \\
 &= |\vec{V}_2|^2 \int [\cos(\theta + \tau) * \cos \psi]^2 \sin \theta \, d\theta \, d\psi : \\
 & \quad |\vec{V}_1|^2 \int [\cos(\theta) * \cos \psi]^2 \sin \theta \, d\theta \, d\psi \qquad \text{Eq. S5} \\
 &= |\vec{V}_2|^2 * \left(\frac{3}{2} - \frac{\cos 2\tau}{2}\right) : |\vec{V}_1|^2
 \end{aligned}$$

In this case, the only condition that generates an identical peak ratio to FTIR is when $\tau = n * \pi, n \in 0 \text{ or } \mathbb{N}$. In this case, the two modes point in identical or opposite directions. Based on DFT calculation, this is very unlikely the case. However, if the molecule is somehow ordered, the angle τ would not be limited to certain angles. The fact that we can measure a non-zero SFG signal agrees with the ordered case.

3.3 - Determination of Absolute Orientation

In 2D SFG experiments, the sign of the signal intensity (I) for a particular vibrational mode is dependent on the orientation of the molecule. This can be seen from the following relationship that relates the signal to the fourth-order susceptibility, $\chi^{(4)}$.¹⁶

$$\begin{aligned}
I_{p,q} \propto \chi_{IJKLM}^{(4)} &= \langle R_{Ii}R_{Jj}R_{Kk}R_{Ll}R_{Mm} \rangle \cdot \alpha_{q,ij}\mu_{q,k}\mu_{p,l}\mu_{p,m} \\
&= \langle R_{Ii}R_{Jj}R_{Kk}R_{Ll}R_{Mm} \rangle \cdot \beta_{ijklm}^{(4)}
\end{aligned}
\tag{Eq. S6}$$

As we described in Eq. S6, the fourth-order molecular response $\beta_{ijklm}^{(4)}$ will have its sign determined by the interplay of the sign of the transition dipole moment vector μ and the Raman tensor α . The sign of $\chi^{(4)}$ will also depend on how the molecule is oriented in the lab-frame, which is given by the rotational matrix component.

The absolute sign of $\chi^{(4)}$ can only be measured in a heterodyne detected experiment where $\chi_{res}^{(4)}$ is interferometrically detected with a reference field, such as a non-resonant signal $\chi_{non-res}^{(2)}$. However, experimentally it can be complicated to measure the absolute sign of $\chi^{(4)}$ because any phase shift between the non-resonant and resonant signals, $\chi_{non-res}^{(2)}$ and $\chi_{res}^{(4)}$, will also influence the measured sign of the signal.

When the experiment is carried out on a metallic surface such as gold, the phase shift between the non-resonant and resonant signals depends on the wavelength of the visible light pulse.¹⁷ Instead of measuring the exact phase shift for our particular setup, we use a molecule with a known surface orientation to determine the sign of our signal. Our approach is to measure the sign of the signal produced from our calibrant molecule and also simulate the 2D SFG spectrum of that molecule in the known orientation to determine the sign relationship between our experimental setup and simulations.

We chose to use para-mercaptobenzoic acid (pMBA) to calibrate our system (Fig. S5). This molecule is useful because it has a C=O stretching mode at about 1740 cm^{-1} .^{18,19} Para-mercaptobenzoic acid forms a covalent bond with gold through its thiol group and has been measured to orient on the surface with a 30° tilt from surface normal, as shown in Fig. S5²⁰. We prepared a pMBA monolayer on gold according to the procedure that produces monolayers with 30° tilt angle²⁰. A gold chip was soaked in a 1 mM solution of pMBA in pure ethanol for 24 hours. Afterward, the chip was removed and rinsed with pure ethanol before drying with N_2 .

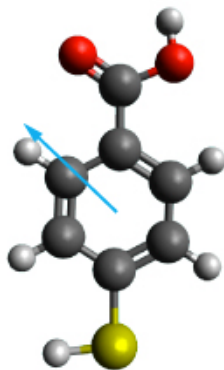


Figure S5: Para-mercaptobenzoic acid optimized geometry and transition dipole moment vector of C=O stretching mode.

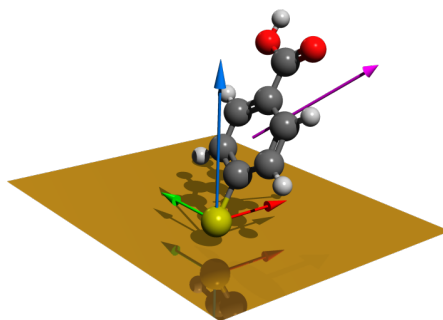


Figure S6: Surface orientation of pMBA. The ring plane is tilted 30° from surface normal.

A 2D SFG spectrum was collected in the same manner as described for the oligo(dT) monolayers. The t_i period was scanned from 0:50:1500 fs and a rotating wave frequency of 1500 cm^{-1} was used. The 2D SFG spectrum of pMBA is shown in Fig. S6.

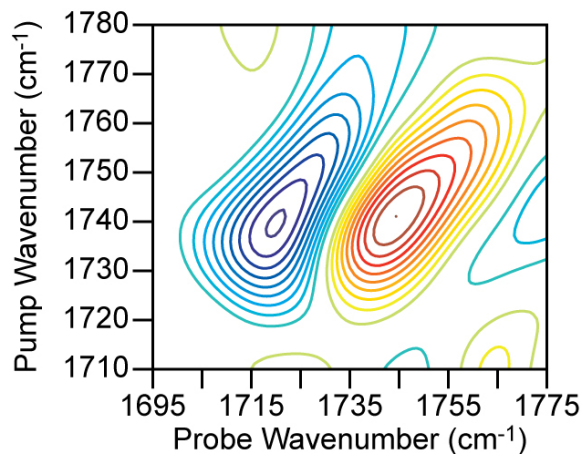


Figure S7: 2D SFG spectrum of para-mercaptobenzoic acid monolayer on gold.

The 2D SFG spectrum of pMBA shows a positive fundamental peak along the diagonal. The overtone is of opposite sign and shifted to lower frequency along the probe axis.

In addition, we have simulated the 2D SFG spectrum of pMBA in the surface orientation shown in Fig. S2. To do this, we performed DFT calculations using Gaussian '09 with the B3LYP functional and 6-311G(d,p) basis set to determine the transition dipole moment vector direction and Raman tensor for the C=O stretching mode of pMBA (Fig. S4)³. The simulated spectrum is shown in Fig. S7.

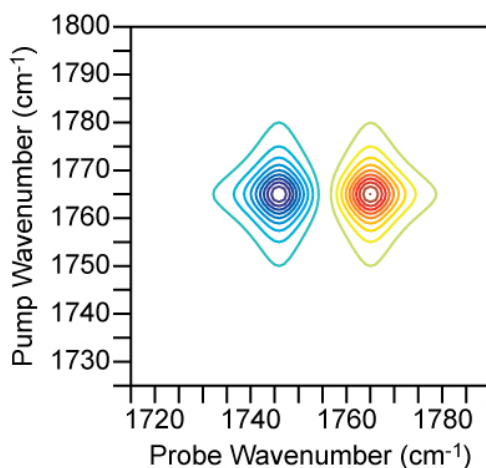


Figure S8: Simulated 2D SFG spectrum of para-mercaptobenzoic acid with surface orientation shown in Fig. S6.

When pMBA has a 30° tilt, the simulated 2D SFG spectrum gives a positive fundamental peak along the diagonal (Fig. S7). Thus, the same sign is given in both the experiment and the simulation for the same pMBA surface orientation. Also, the sign of the simulated spectrum does not vary with small changes in tilt angle. In fact, the tilt angle can range from 0° to 90° without the spectrum changing sign.

From the experimental spectrum and simulation of pMBA, we know that matching orientations between the two cases will give spectra that have the same signs. With this known, we can now match the signs in the experimental and simulated spectra of the oligo(dT) monolayer, and find the absolute orientation of the thymine bases.

3.4 - 2D SFG Absolute Signal Size

The absolute signal sizes for the 2D SFG experiments shown in the main text Fig. 5 are shown below. Cuts at constant pump frequency across the T1 and T2

modes are presented in Fig. S9.

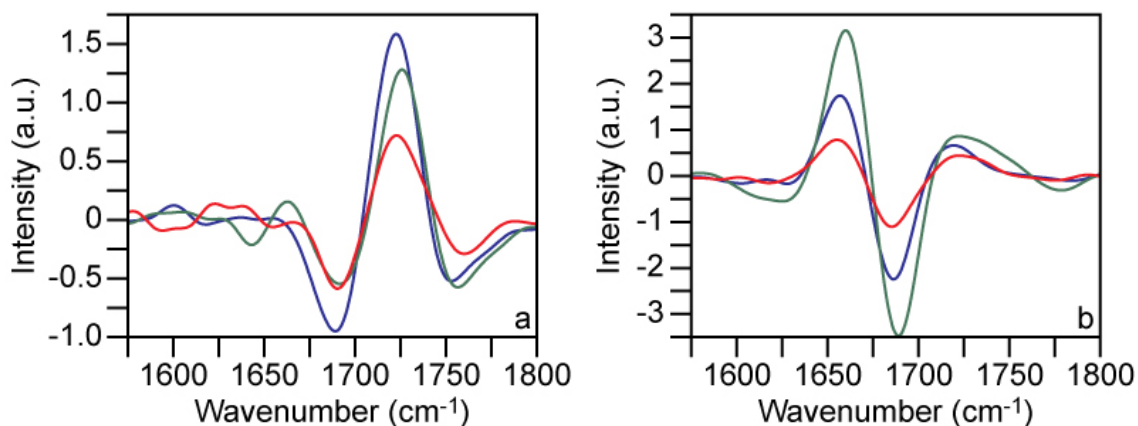


Figure S9: 2D SFG signal size comparison for oligo(dT) monolayers. (a) Cut along T1 mode ($\omega_{\text{pump}} = 1715 \text{ cm}^{-1}$). (b) Cut along T2 mode ($\omega_{\text{pump}} = 1672 \text{ cm}^{-1}$). In both (a) and (b), (dT₁₀)-SH (red), (dT₁₅)-SH (green), and (dT₂₅)-SH (dark blue) are shown.

Although we use gold as substrate, we did not see any evidence that the gold surface enhances the signal. Gold nanorods with proper size and shape can enhance specific frequencies,²¹ but flat gold surfaces have much smaller enhancements. Moreover, the linker has six C-C bonds separating the surface from the oligomers, which should also reduce electric field effects on the bases closest to the gold surface.

3.5 - 1D SFG Absolute Signal Size

The absolute signal sizes for the 2D SFG experiments are subject to intensity fluctuations in the mid-IR pump pulses and require longer scanning periods over which laser fluctuations occur. For these reasons, we also compared 1D SFG signal size for oligo(dT) monolayers of various length collected within hours to minimize laser changes. Two (dT)₁₀-SH and two (dT)₂₅-SH samples were prepared under identical conditions (samples A and B) to demonstrate possible sample-to-sample fluctuations in signal size.

The 1D SFG signal contains both resonant signal from oligo(dT) and non-resonant signal from the gold surface (Fig. S10). To isolate the 1D SFG resonant signal from oligo(dT), a bare gold non-resonant spectrum was collected and subtracted from the oligo(dT) spectra. The resonant 1D SFG signal from the oligo(dT) monolayer are shown in Fig. S10. These spectra show that the T2 mode gives a positive peak in the spectrum at $\sim 1670 \text{ cm}^{-1}$ and the T1 mode gives a negative peak at $\sim 1730 \text{ cm}^{-1}$.

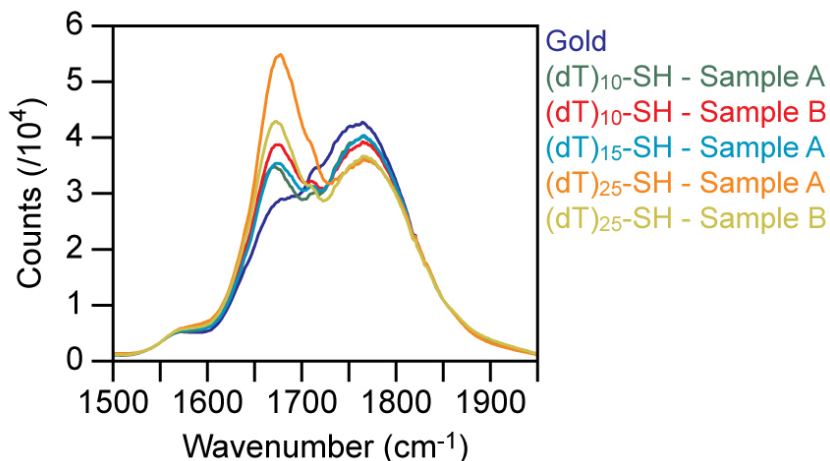


Figure S10: 1D SFG spectra of oligo(dT) monolayers on gold. The spectrum from a bare gold sample (dark blue) gives the non-resonant background contribution. Oligo(dT) monolayer samples contain resonant signal from thymine bases and non-resonant signal from gold. All spectra are scaled to match the gold sample intensity at 1550 cm^{-1} and 1850 cm^{-1} using a linear scaling across the spectral range for best comparison.

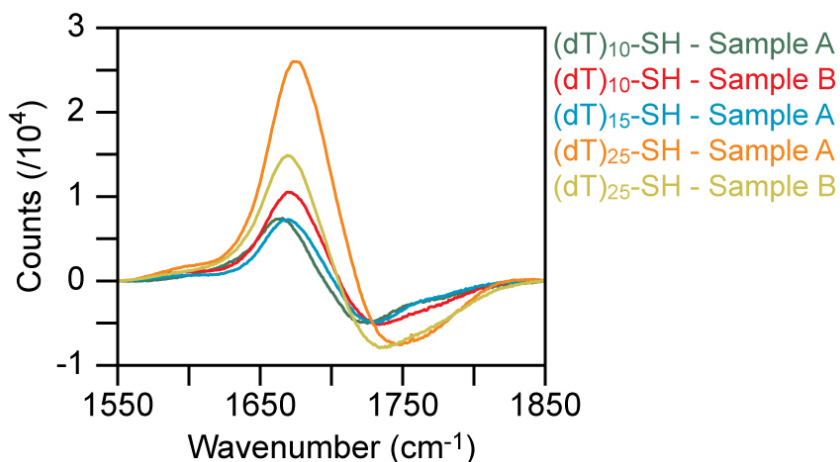


Figure S11: Resonant 1D SFG spectra of oligo(dT) monolayers on gold. The resonant contribution for each sample is isolated from the non-resonant background by subtracting the gold spectrum from all oligo(dT) spectra in Fig. S7.

Here is an interesting observation when compare the SFG to XPS result in section 2.1.2. The intensity variation could be large even for identical sample with small difference in surface coverage. This is because SFG signal is both a function of surface coverage and molecule orientation. From table S2 we know that the surface coverage changes within less than $\sim 5\%$ where the SFG intensity could vary as much as 40% in Fig. S11. SFG is sensitive enough to pick-up slight orientation change induced by small change in surface coverage. To decide the exact orientation of different sample, one can take 2D SFG spectrum and

determine the tiny orientation change by 2D SFG spectral simulation. The structure of the order strands is the same regardless of surface coverage, which we can conclude because of 2D SFG spectral features are nearly identical.

3.6 - Simulated 2D SFG Absolute Signal Size as Function of ψ

The 2D SFG signal intensity depends on the lab frame projection of transition dipoles and Raman tensors. Thus the intensity also depends on the angle ψ that is defined in Fig. 7a. For all the orientations that satisfy the outlined experimental criteria (blue dots Fig. 7b), we have plotted the intensity of the T1 fundamental peak in Fig. S12. The intensity of the T2 fundamental peak follows a very similar trend. As can be seen in Fig. S12, the highest signal intensity is given when $\psi \sim 90^\circ$ because this orientation gives large projections of the transition dipole moment vectors and Raman tensor on the z-axis.

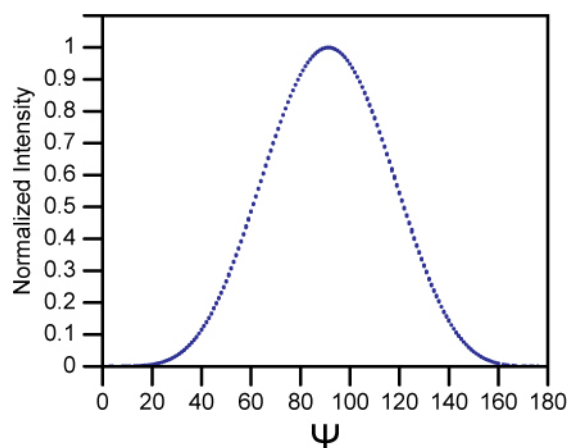


Figure S12: Simulated 2D SFG signal intensity of T1 fundamental peak as a function of twist angle ψ .

3.7 - Peak Sign and Intensity Analysis of HD 2D SFG

According to Eq. S6, if the molecular orientation distribution is a delta function, its 2D SFG signal intensity is proportional to the product of Raman tensor and transition dipole elements. Assuming that all laser beams are p -polarized with 90° incident angles, only the Raman tensor and transition dipole components perpendicular to the surface are probed (i.e. α_{zz} and μ_z). This is assumed in the following analysis. Also, to avoid interference effects between the fundamental and overtone peaks, we only consider one-exciton rephasing pathways. Under these assumptions the peak intensities for a simplified 2D SFG spectrum with two modes (Fig. 6a) are given by Eq. 1-3.

From Eq. 1-3, we see that the sign of each peak is determined by the product of the Raman tensor and transition dipole of the probed mode (final two

interactions). For instance, both the sign of diagonal peak I_{AA} and the sign of the cross-peak I_{BA} depend only on the sign of $\alpha_{A,ZZ} \cdot \mu_{A,Z}$. As a result, the peaks with the same probing mode will have the same sign. We also found that, unlike a typical 2D IR spectrum, the intensity of cross-peak pairs (I_{AB} and I_{BA}) can be different since the final interaction is a Raman tensor, which provide asymmetric signal intensity. In 2D IR, the cross-peak intensities are always symmetric ($I_{AB} = I_{BA} \propto \mu_A^2 \times \mu_B^2$).

In sum, we found that there are four kinds of 2D SFG peak patterns for a coupled two modes (A, B) system shown in Fig. S13.

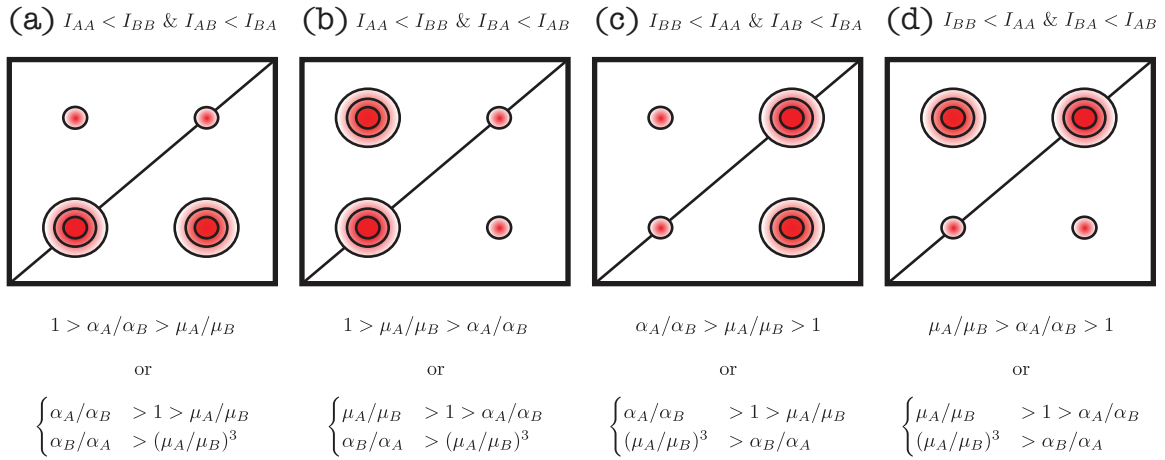


Figure S13: All possible peak patterns for a simplified 2D SFG spectrum with two modes A and B. The equations below each peak pattern shows the corresponding conditions of the two modes system.

From Eq. 1-3 we can calculate the relative peak intensities between diagonal and cross peaks:

$$\frac{I_{AA}}{I_{BB}} \propto \left(\frac{\alpha_{A,ZZ}}{\alpha_{B,ZZ}} \right) \cdot \left(\frac{\mu_{A,Z}}{\mu_{B,Z}} \right)^3 \quad \text{Eq. S7}$$

$$\frac{I_{AB}}{I_{BA}} \propto \left(\frac{\alpha_{B,ZZ}}{\alpha_{A,ZZ}} \right) \cdot \left(\frac{\mu_{A,Z}}{\mu_{B,Z}} \right) \quad \text{Eq. S8}$$

The relative strength between the lab frame projection of Raman tensors and transition dipoles determine which pattern of 2D SFG a system possess. We summarized the conditions for each of the corresponding peak pattern in Fig. S13.

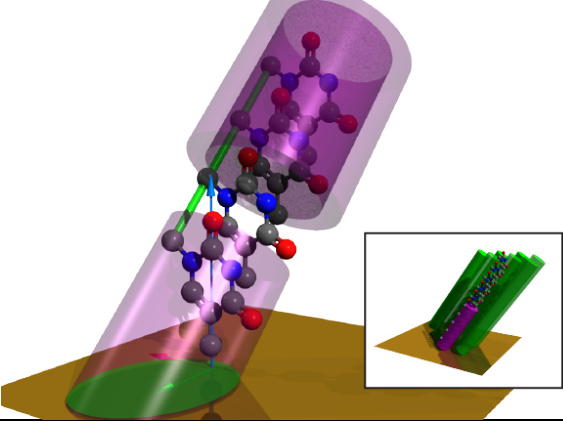
In our previous paper¹⁶, we showed that a SFG inactive mode can be observed through its cross peak with an SFG active mode. This is a special case when the mode is Raman inactive ($\alpha_A = 0$ or $\alpha_B = 0$) as shown in Fig. S13b or S13c.

Interestingly, if the intensity ratios between peaks can be measured accurately in a 2D SFG experiment (i.e. accounting for peak overlap and interference), then the ratio between corresponding projections of Raman tensors and transition dipoles can be accurately determined. In this case, we can extract the surface specific IR and Raman information in one experiment.

3.8 - Footprint Estimation of Monolayer Film

According to the two tables S1 and S2, the DNA coverage is about 0.5~1 molecule/nm². That means the footprint of each molecule is about 1~2 nm². To estimate the size of the footprint for a ssDNA strand, here we defined two types of footprint and calculate their corresponding values.

Assuming the ssDNA strand is a rigid rod, the size of surface cross-section only depends on the rod radius (R) and the rod tilting angle (θ). Depending on how the molecules are packed, we defined the footprint in two extreme cases: the area of the cross-section (densely packing model) or the projected area of the whole strand (loosely packing model). Fig S14 shows the estimated footprints of a rod with 3~4 Å radius and 50 degrees tilting angle. The top row refers to a dense packing model where all strands lean on each other while the bottom row is the footprint for a loosely packing model where each strand occupies its projected area.

Different packing models	Footprint, $R = 3 - 4 \text{ \AA}, \theta = 50^\circ$
	$Area = \frac{\pi * R^2}{\sin \theta}$ <p><i>R: radius of enclosing cylinder</i> <i>θ: angle between cylinder axis and gold surface</i></p>
densely packing model	Area = 0.36 - 0.65 nm ²

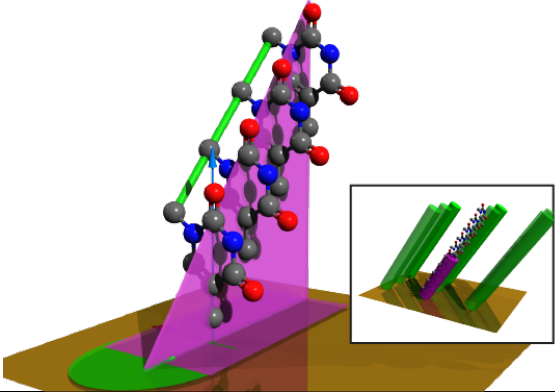
	$\text{Area} = \text{Green} + \text{Purple}$ $\text{Purple} = 2R * L$ $L = \frac{Z}{\tan \theta}$ $Z = 5.5782 + (N - 1) * 3.5 * \cos \theta \text{ (\AA)}$ <p>N: number of bases</p>
loosely packing model	Area = 0.77 – 1.11 nm ²

Figure S14: Comparison between the two definitions of footprint. The top row is the footprint definition for the densely packing model; the bottom row is the definition for loosely packing model. The insertions show how these rods packed. Each green rod representing a ssDNA strand.

For the densely packing model, the footprint only depends on the cross section of the rod, not chain length. We calculate the footprints for different tilting angles in Fig S15. The footprint is much smaller than experimental observations (1~2 nm²).

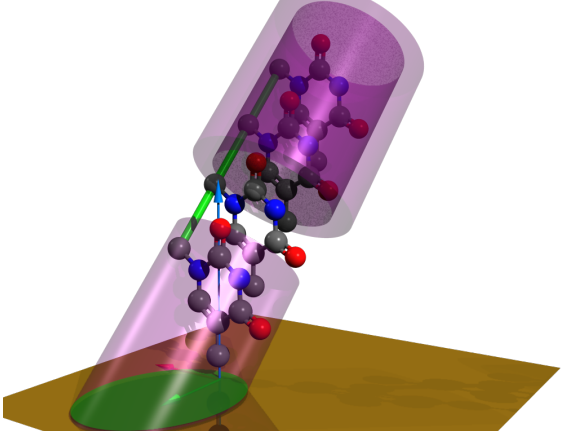
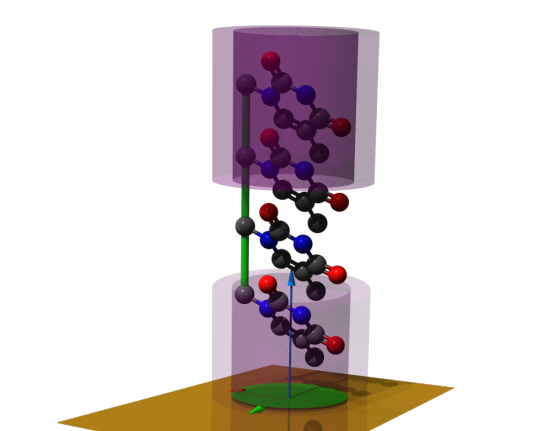
Dense packing condition 1	Dense packing condition 2
	
Area = 0.36 - 0.65 nm ² R = 3 - 4 Å, θ = 50°	Area = 0.29 - 0.51 nm ² R = 3 - 4 Å, θ = 90°

Figure S15: Different tilting angle for densely packing model. The value below each figure refers to footprint area (Area), radius of enclosing cylinder (R), and tilting angle of DNA backbone (θ). The green interception indicates the estimate footprint.

In the loosely packing model, the footprint is a function of strand length. E.g., the longer the chain is, the larger the footprint is. This is due to inclusion of the

projection part of ssDNA strand. With tilting angle of 50 degrees, we calculate footprints for each of different chain length and summarize in table S5.

# Bases	Footprint (nm^2)
10	1.41 - 1.97
15	1.95 - 2.68
25	3.02 - 4.11

Table S5: The footprint area for the second model for different chain length.

If the monolayer is loosely packed, the surface coverage should decrease linearly with increase of chain length. Although the correlation does exist, the dependency is not linear and the model footprints are higher than experiments. Since the real ssDNA molecule is not a rigid rod, the packing condition of the monolayer likely lies in between the two models.

Supplemental Information References

- (1) Laaser, J. E.; Skoff, D. R.; Ho, J.-J.; Joo, Y.; Serrano, A. L.; Steinkruger, J. D.; Gopalan, P.; Gellman, S. H.; Zanni, M. T. *J. Am. Chem. Soc.* **2014**, *136*, 956–962.
- (2) Laaser, J. E.; Xiong, W.; Zanni, M. T. *J. Phys. Chem. B* **2011**, *115*, 2536–2546.
- (3) Frisch, M. J.; Trucks, G. W.; Schlegel, H. B.; Scuseria, G. E. *Gaussian 09, revision D. 01; Gaussian, Inc; Wallingford CT, 2009.*
- (4) Vázquez, J.; Stanton, J. F. *Molecular Physics* **2007**.
- (5) Greenler, R. G. *J. Chem. Phys.* **1966**, *44*, 310.
- (6) Greenler, R. G.; Snider, D. R.; Witt, D.; Sorbello, R. S. *Surface Science* **1982**, *118*, 415–428.
- (7) Demirdöven, N.; Khalil, M.; Tokmakoff, A. *Phys. Rev. Lett.* **2002**, *89*, 237401.
- (8) Ge, N. H.; Zanni, M. T.; Hochstrasser, R. M. *J. Phys. Chem. A* **2002**.
- (9) Petrovykh, D. Y.; Kimura-Suda, H.; Tarlov, M. J.; Whitman, L. J. *Langmuir* **2004**, *20*, 429–440.
- (10) Peng, C. S.; Jones, K. C.; Tokmakoff, A. *J. Am. Chem. Soc.* **2011**, *133*, 15650–15660.
- (11) Greve, C.; Elsaesser, T. *J. Phys. Chem. B* **2013**, *117*, 14009–14017.
- (12) Li, D.; Fedeles, B. I.; Singh, V.; Peng, C. S.; Silvestre, K. J.; Simi, A. K.; Simpson, J. H.; Tokmakoff, A.; Essigmann, J. M. *Proc. Natl. Acad. Sci. U.S.A.* **2014**, *111*, E3252–E3259.
- (13) Bredenbeck, J.; Ghosh, A.; Nienhuys, H.-K.; Bonn, M. *Acc. Chem. Res.* **2009**, *42*, 1332–1342.
- (14) Banyay, M.; Sarkar, M.; Gräslund, A. A Library of IR Bands of Nucleic Acids in Solution. *Biophys. Chem.* **2003**, *104*, 477–488.
- (15) Lee, C.; Park, K.-H.; Cho, M. *J. Chem. Phys.* **2006**, *125*.
- (16) Laaser, J. E.; Zanni, M. T. *J. Phys. Chem. A* **2013**, *117*, 5875–5890.
- (17) Potterton, E. A.; Potterton, E. A.; Bain, C. D.; Bain, C. D. *Journal of Electroanalytical Chemistry* **1996**, *409*, 109–114.
- (18) Wells, M.; Dermody, D. L.; Yang, H. C.; Kim, T.; Crooks, R. M.; Ricco, A. *J. Langmuir* **1996**, *12*, 1989–1996.
- (19) Rosendahl, S. M.; Burgess, I. J. *Electrochimica Acta* **2008**, *53*, 6759–6767.
- (20) Lee, J. R. I.; Lee, J. R. I.; Willey, T. M.; Willey, T. M.; Nilsson, J.; Nilsson, J.; Terminello, L. J.; Terminello, L. J.; De Yoreo, J. J.; De Yoreo, J. J.; van Buuren, T. *Langmuir* **2006**, *22*, 11134–11141.
- (21) Link, S.; El-Sayed, M. A. *J. Phys. Chem. B* **1999**, *103*, 8410–8426.